Investigation of the $2p_{3/2}$-$3d_{5/2}$ line emission of Au^{53+}–Au^{69+} for diagnosing high energy density plasmas

G. V. Brown, S. B. Hansen,* E. Träbert,† P. Beiersdorfer, K. Widmann, H. Chen, H. K. Chung, J. H. T. Clementson, M. F. Gu, and D. B. Thorn

Lawrence Livermore National Laboratory, Livermore, California 94550-9234, USA

(Received 5 February 2008; published 23 June 2008)

Measurements of the *L*-shell emission of highly charged gold ions were made under controlled laboratory conditions using the SuperEBIT electron beam ion trap, allowing detailed spectral observations of lines from Fe-like Au^{53+} through Ne-like Au^{69+}. Using atomic data from the Flexible Atomic Code, we have identified strong $3d_{5/2} \rightarrow 2p_{3/2}$ emission features that can be used to diagnose the charge state distribution in high energy density plasmas, such as those found in the laser entrance hole of hot hohlraum radiation sources. We provide collisional-radiative calculations of the average ion charge $\langle Z \rangle$ as a function of temperature and density, which can be used to relate charge state distributions inferred from $3d_{5/2} \rightarrow 2p_{3/2}$ emission features to plasma conditions, and investigate the effects of plasma density on calculated *L*-shell Au emission spectra.

DOI: 10.1103/PhysRevE.77.066406 PACS number(s): 52.70.La, 32.30.Rj, 52.38.Ph

I. INTRODUCTION

Producing a hot radiation environment that can be used for studies of material under extreme conditions and possibly in local thermodynamic equilibrium (LTE) has been one of the central goals of high energy density physics. Recent experiments using four of the planned 196 beams of the National Ignition Facility (NIF) at the Lawrence Livermore National Laboratory and at the Omega laser at the University of Rochester's Laboratory for Laser Energetics have demonstrated the production of radiation temperatures as high as 340 eV [1,2]. Scaling laws [3] predict even higher temperatures when NIF attains full power or when the Laser Mega-Joule (LMJ) in France comes online.

The creation of extremely hot radiation environments has been achieved by depositing the available laser energy in the smallest possible space enclosed by walls of high-Z material. The walls, typically made of gold, form a hohlraum with only one opening, i.e., the laser entrance hole, through which the laser light enters. The laser light is absorbed by the wall and ionizes the wall material. The resulting plasma reradiates a large fraction of the deposited laser energy and thus fills the hohlraum with intense soft x radiation.

Unlike the large-scale hohlraums employed for inertial confinement fusion, reduced-size "hot" hohlraums fill with plasma on the time scale of the laser pulse. Plasma even spills out of the laser entrance hole and interacts with the laser light. This laser-plasma interaction transfers energy between the laser beams and tends to deflect the beams from entering the hohlraum. The laser-plasma interaction outside the laser entrance hole limits the amount of laser energy that can be deposited into a reduced-size hohlraum [1,2]. A critical parameter in understanding the laser-plasma interaction is the electron temperature of the plasma outside the laser entrance hole. Hydrodynamic calculations have predicted temperatures around 20 keV, although temperatures as high as 30 keV might be possible under some circumstances. Initial Thomson scattering measurements have indicated temperatures as high as 50 keV but have been subject to large uncertainties because of a lack of knowledge of the average ionization state of the gold plasma.

Gold plasmas with temperatures of tens of keV will emit significant amounts of *L*-shell radiation, and at such high temperatures the dominant charge state is likely to be Ne-like Au^{69+}. The emission of high-*Z* Ne-like ions is dominated by the $(1s^2 2s^2 2p^5_{3/2} 3d_{5/2})_{J=1} \rightarrow (1s^2 2s^2 2p^6)_{J=0}$ transition, commonly labeled $3D$ [4]. The emission of the neighboring ions is also dominated by $3d_{5/2} \rightarrow 2p_{3/2}$ transitions, as intimated in a few measurements of near-Ne-like high-*Z* ions, where the corresponding transitions from ions with lower charge, such as Na-, Mg-, and Al-like ions, were seen to form a "picket-fence" pattern [4,5]. In this case, the emission from one charge state is rather well separated from that of its neighbor. This picket-fence pattern is thought to extend to even lower charge states below the Al-like charge state, i.e., similar to the pattern observed for *M*-shell transitions of gold and tungsten [6–8] in earlier electron beam ion trap (EBIT) experiments and for *L*-shell Au transitions in laser plasmas [9,10]. The shape of this pattern depends on the abundance of the emitting ions from each charge state and thus on the ionization balance. The charge balance, in turn, depends on the electron temperature. This radiation pattern, therefore, can, in principle, serve as a means for determining both the average ionization state of the plasma as well as its electron temperature if the emission features from individual ions are understood.

The challenge of accurately modeling complex ions in non-LTE is well known [11–13]. Reliable collisional-radiative models require accurate knowledge of atomic structure and transition rates of spontaneous, collisional, and radiatively driven processes and the inclusion of all relevant channels of population transfer. The difficulty of developing accurate and efficient collisional-radiative models has hindered the development of plasma diagnostics based on complex many-electron ions far from closed shells. To better un-

*hansen50@llnl.gov

†Also at Fakultät für Physik und Astronomie, Ruhr-Universität Bochum, D-44780 Bochum, Germany.

derstand the non-LTE emission from such ions and to develop it as a diagnostic for high energy density plasmas, we have pursued a two-pronged effort. First, we have experimentally studied the $3d_{5/2} \rightarrow 2p_{3/2}$ emission pattern of highly charged gold ions in the SuperEBIT electron beam ion trap at the Lawrence Livermore National Laboratory under well controlled laboratory conditions. The adjustable beam energy of the device allows us to step through the charge states, enabling unambiguous identification of the strong *L*-shell lines and line blends. In the present work, we identify *L*-shell spectral features of Au^{53+} through Au^{69+} (Ne- through Fe-like ions), which can be used to determine the emitting charge state distributions (CSD) of gold in high energy density plasma experiments. We indeed find a picket-fence pattern which persists for charge states far from Ne-like gold. Complementing the experimental effort, we have performed collisional-radiative calculations to confirm experimental line identifications, correlate the measurable average ion charge with plasma temperature and density, and predict density-sensitive emission signatures of Au *L*-shell emission. This allows us to extend the validity of our findings to the high densities found in high energy density plasmas. In the low-density plasma regime, the CSD is almost entirely controlled by the electron temperature and can be a sensitive plasma thermometer. At higher plasma densities, both temperature and density affect the CSD, complicating CSD-based diagnostics and necessitating identification of density-sensitive emission signatures.

II. EXPERIMENTAL DATA

The experiment was performed at the SuperEBIT electron beam ion trap [14] at the Lawrence Livermore National Laboratory. SuperEBIT is the first such device built and has been optimized for spectroscopic studies of highly charged ions [15], including the study of spectra needed for diagnosing high energy density plasmas [16].

Au was supplied to the ion trap from the ablation plume of a laser injection system [17]. The laser fired about every two seconds to replenish the material in the trap, where it was quickly ionized by the electron beam. Every 19 s the content of the trap was dumped to halt the accumulation of possible contaminants, such as barium and tungsten, and then the trap cycle was repeated. X-ray emission from the ions in the trap was detected by means of a cryogenic microcalorimeter built by the Goddard Space Flight Center [18–20] with $32\,624 \times 624$ μm^2 HgTe absorbers ("pixels"), of which 24 were read out for this experiment. For the present application, the microcalorimeter was operated at a slightly higher temperature ($T=65$ mK) than usual for this instrument in order to record x rays with energy as high as 18 keV. After a rough calibration of all pixels with their amplifier chains, the individual signals were combined. For single x-ray transitions at 8 to 10 keV, a linewidth [full width at half maximum (FWHM)] of about 10 eV was found, which implies a resolving power of about 900. Measured spectral features with larger linewidths (15 to 18 eV) thus reveal the presence of line blends. For these experiments, the typical count rates on the microcalorimeter array were 1–1.5 counts per second per pixel. At these rates, there is no significant loss from the pulse pileup [21,22].

The individual pixel pulse height was calibrated against $n=1-2$ lines of He- and H-like ions of Ar (near 3.3 keV), Ni (7.7–8.1 keV), and Ge (10.2–10.6 keV) [23,24]. Ar was supplied via a ballistic gas injector, Ni as a gas [nickelocene, that is bis(cyclopentadienyl)nickel(II)] from a sublimation injector, and Ge from the laser injector. For the calibration spectra, the electron beam energy was increased to up to 80 keV and the electron beam current run at 130 mA. Light element gases (N_2) were also injected at times (at very low pressure) with the Au measurements to provide a coolant for the stored ion cloud. When injecting Ni, the disintegrating nickelocene molecule provided sufficient amounts of light ion species so that the regular cooling gas supply could be paused. Typical electron beam currents were around 110 mA.

The experiment primarily aimed to measure the 2–3 transitions of Au emitted in the x-ray energy range from 9 to 12 keV. The highest charge state of interest was Au^{69+} (Ne-like) with its closed $n=2$ shell ground state. This ion has an ionization potential (IP) of 18 keV [25], which was chosen as the highest electron beam energy used in the measurements. The ionization potential of the next lower charge state [Au^{68+} (Na-like)] is 8.4 keV, and those of the ions with more electrons are even lower [for example, the IP of Au^{53+} (Fe-like) is only 5.2 keV]. However, the IP refers to the valence electron ($n=3$ for all of those ions below the Ne-like ion), whereas the x-ray transitions in the aforementioned x-ray range relate to inner-shell excitation.

The microcalorimeter is equipped with four thin filters (Al on polyimide) to protect it from thermal radiation that would heat the array. The four filters have a total thickness of 360 nm of Al (absorption 30% to 0.1% in the energy range 1.6 to 15 keV) and 400 nm of polyimide (absorption few percent to 0.01%); these absorption values are derived from information on the web pages of the Berkeley Center for X-ray Optics (CXRO) [26]. Also in the light path between SuperEBIT and the microcalorimeter was a Be window of 12.7 μm thickness, with absorption varying from 0.16% at 8.5 keV to 0.06% at 12.5 keV x-ray energy. The quantum efficiency of the HgTe absorbers in the detector varies significantly over the range of the present observations: from near unity at x-ray energies lower than 5 keV to 0.75 at 8.5 keV to 0.415 at 12.284 keV. Above this edge, the quantum efficiency jumps to 0.621 and then drops again, to 0.56 at 13 keV. Corrections for both filter and detection efficiency have been applied to the raw data in the plots presented here.

Figure 1 shows measured emission spectra for three electron beam energies. The spectra were calibrated against reference lines of H- and He-like ions of Ar, Ni, and Ge. The principal Ni lines (Table I) also appear in most of the Au spectra and serve as a monitor of the calibration quality. The strongest lines of Au^{69+} (Ne-like) suffer the least from blending with other charge states; their positions can be compared to high-accuracy measurements [28] that have been made with crystal spectrometers, and the agreement of our lower-resolution data with those reference lines is excellent (see Table II). The Au emission shown in Fig. 1 is strongly dependent on the beam energy: as E_{beam} decreases, the major

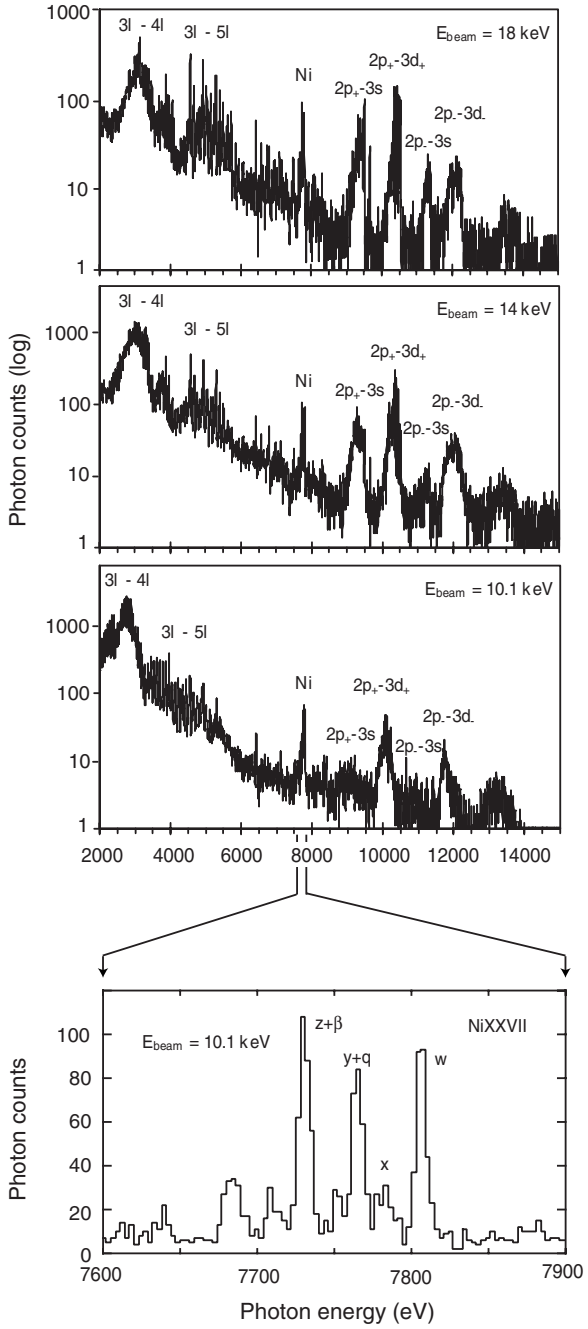

FIG. 1. Broadband x-ray spectra of Au on a logarithmic signal scale at three electron beam energies. The positions of the dominant Au emission line groups and the Ni calibration lines are marked. At bottom, a detailed spectrum of the calibration lines of He-like Ni at 14 keV electron beam energy demonstrates the spectral resolving power of the microcalorimeter.

emission features shift to lower energies and the $(2p_+ - 3s)/(2p_+ - 3d_+)$ and $(3l-5l)/(3l-4l)$ intensity ratios decrease.

The trends in the *L*-shell emission are seen more clearly in Fig. 2, where the dominant *L*-shell features recorded from different beam energies are shown. For each $nlj-n'l'j'$ transition type, the emission features associated with individual charge states are separated by about 40 eV. The picket-fence structure intimated by earlier high-*Z* *L*-shell spectral measurements is thus confirmed and, in the case of the $3d_{5/2} \rightarrow 2p_{3/2}$ emission features, extends to Fe-like Au^{53+}, as shown in the bottom spectrum of Fig. 2. The highest energy peak of each transition type belongs to the Ne-like ion. These sharp lines have little overlap with features from neighboring charge states. The $3d_{5/2} \rightarrow 2p_{3/2}$ features from multiple lower charge states are also remarkably distinct, with minimal line blending for charge states above about *V*-like Au^{56+}, as our calculations in the next section will show. Although describing the blended emission features of lower charge states may require full modeling, in higher-temperature plasmas where the average ion charge $\langle Z \rangle$ is well above 56+, the $3d_{5/2} \rightarrow 2p_{3/2}$ features provide a reasonably good indication of the charge balance even in the absence of detailed modeling.

There is a significant change in the *L*-shell emission spectra between beam energies of 11.65 keV and 13 keV, as the Au ions pass the partially closed-shell Ar-like ion (IP =6.7 keV). We note also that spectra from lower electron beam energies include emission above the beam energy (see especially the E_{beam}=10.1 keV in Figs. 1 and 2), demonstrating that direct collisional excitation is not the only process giving rise to the high energy emission. A portion of the emission at energies greater than the beam energy can be attributed to radiative recombination processes, but there remain significant contributions to the spectra at the positions of the expected *L*-shell line emission above the beam energy. (Even at an electron beam energy of 8.28 keV, a band of lines near 8.7 keV and some weak lines near 10.2 keV are to be seen.) Dielectronic recombination into exotic multiply excited states is the most likely source of these emission lines.

TABLE I. Ni^{26+} (He-like) ion reference lines [24] used for calibration. The line label notation follows Gabriel [27].

Line	Energy (eV)
w	7805.562
x	7765.667
y	7752.299
z	7731.588

TABLE II. Au^{69+} (Ne-like) line energies in eV (±3 eV) from the present measurements. Calculated values for transitions energies were obtained using the Flexible Atomic Code (FAC) [37]. The line labels follow the scheme given by Beiersdorfer *et al.* [5]. Note: *M*2 and 3*G* are not resolved in the calorimeter spectra.

Line	Transition	Calculated (this work)	Measured (this work)
*M*2	$2p_{3/2}$-$3s_{1/2}$	9491.9	9505
3*G*	$2p_{3/2}$-$3s_{1/2}$	9501.4	9505
*E*2*L*	$2p_{3/2}$-$3p_{1/2}$	9659.0	9666
*E*2*M*	$2p_{3/2}$-$3p_{3/2}$	10189	
3*E*	$2p_{3/2}$-$3d_{3/2}$	10358	
3*D*	$2p_{3/2}$-$3d_{5/2}$	10522	10527
3*F*	$2p_{1/2}$-$3s_{1/2}$	11375	11382
3*C*	$2p_{1/2}$-$3d_{3/2}$	12264	12270

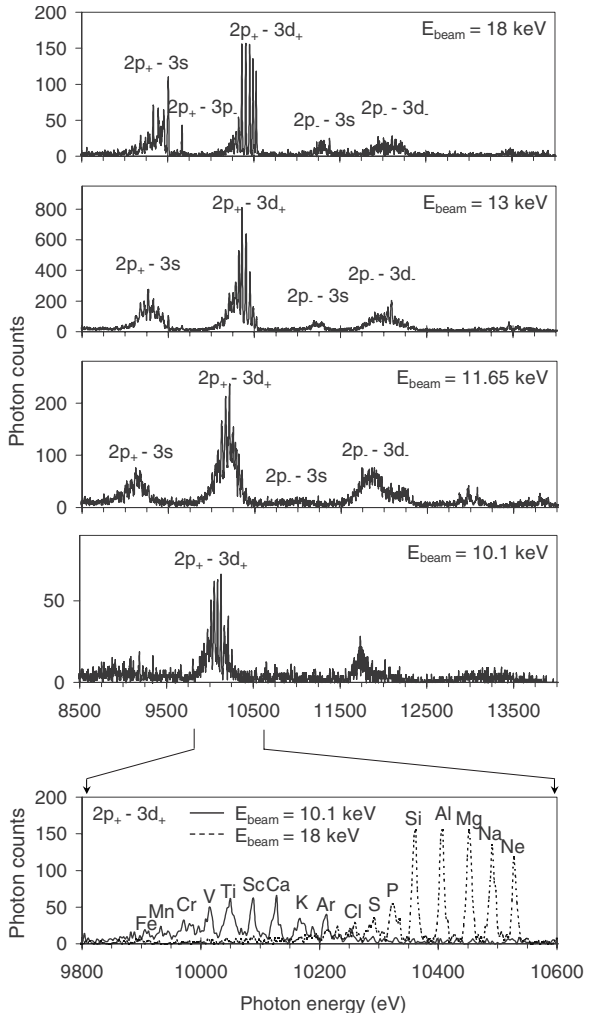

FIG. 2. *L*-shell emission at four electron beam energies. At bottom, an expanded view of $3d_{5/2} \rightarrow 2p_{3/2}$ features from the E_{beam}=10.1 and 18 keV spectra, labeled with the isoelectronic sequence of the dominant parent ion.

III. ATOMIC STRUCTURE AND COLLISIONAL-RADIATIVE CALCULATIONS

Although the atomic structure of the closed-shell Ne-like ion has been well studied for mid-*Z* elements, relatively few calculations have been done for high-*Z* elements such as Au (*Z*=79) (for a discussion, see [29]). Ivanova and Gulov [30] have calculated the level structure of Ne-like ions, but for the heaviest ions (including Au), this covers only n=3 levels. Zhang and Sampson [31–33] have calculated the excitation of n=3 and n=4 levels of Ne- and Na-like ions up to Z =92, and they also covered the production of core-excited Ne-like ions by inner-shell ionization of Na-like ions [34]. More recently, May *et al.* [10] have presented calculations of strong coronal emission lines from Au^{52+}–Au^{69+} ions using the HULLAC atomic structure code [35].

We have used the Flexible Atomic Code (FAC) designed by Gu [36,37] to generate fine-structure atomic levels and rate data for Au ions from H-like (Au^{78+}) to Zn-like (Au^{49+}). The atomic structure and rate data are then used in the collisional-radiative and spectral synthesis code SCRAM to calculate level populations, charge state distributions, and emission spectra. The fine-structure atomic data calculations for all ions include at least the following "coronal" configurations: (1) the ground state configuration, (2) configurations accessible via single excitation from the ground-state valence shell n_{val} to $n \leq n_{val}+1$, and (3) configurations accessible via a single excitation from inner shells of the ground configuration to $n=n_{val}$. Excitations to higher n are included in the closed-shell He-, Ne-, and Ni-like ions. At the low densities of the electron-beam ion trap, where electronic state populations are overwhelmingly concentrated in ground state configurations and line emission tends to be limited by direct collisional excitation and ionization, this set of coronal configurations is generally adequate to describe the major transition lines with reasonable accuracy: the restricted structure is sufficient to account for the dominant configuration interaction effects in each ion, and the extended structure of closed-shell ions ensures that radiative cascades into metastable states are treated properly (absent collisional depopulation, metastable states collect significant population and can give rise to intense emission lines despite their small radiative decay rates).

Although this restricted set of fine structure data suffices at low densities, it fails at higher densities where multistep processes lead to significant population in multiply excited configurations, opening up new channels for population transfer and giving rise to strong satellite emission features from transitions that differ from the coronal resonance lines only in the configuration of spectator electrons. Including all possible permutations of accessible configurations with fine structure detail adds enormous complexity to the atomic structure and leads to computationally intractable models with potentially more than $\sim 10^9$ levels. We have thus developed a hybrid atomic structure scheme in which the fine-structure "coronal" configurations discussed above are supplemented with relativistic configuration averaged levels (nlj terms). The supplementary configurations include all permutations of electrons in the valence n shell, all single excitations from these valence configurations up to $n_{val}+3$, and all double excitations from n_{val} and inner-shell excitations from $n < n_{val}$ up to $n_{val}+1$. Since the term calculations include neither the extensive configuration interaction (CI) effects nor the effects of departures from pure jj coupling that are essential to accurate transition energies and line intensities, we apply "CI" corrections to all transitions of a given $n\ell j - n'\ell' j'$ type. The CI corrections, which include both shifts in transition energies and factors that adjust oscillator strengths and radiative rates, are determined by comparing fine structure transitions and unresolved transition arrays (UTAs) among the coronal configurations. The CI energy shifts are generally stable across ionization stages for a given transition type, as shown in Table III, where the CI shifts are given along with the measured and calculated transition energies of the strongest emission features in the recorded spectra. We note that the CI shift of the $3d_{5/2} \rightarrow 2p_{3/2}$ transitions is approximately equal in magnitude (and opposite in sign) to the UTA shift given by the FAC code, so that it is possible to obtain fortuitous agreement with the experiment if both CI and UTA shifts are excluded.

The hybrid atomic structure approach [38] with CI correction preserves much of the accuracy of fine structure model-

TABLE III. Calculated and measured energies in eV (measured energies are ±3 eV) of prominent *L*-shell spectral features identified by transition type and isoelectronic sequence. The calculated energies are based on fine structure energy levels. The configuration interaction (CI) shifts of the UTAs in the hybrid model discussed in the text are also given (in eV). Asterisks indicate broad features or line blends.

Isoel. sequence	Transition	Measured energy	Calculated energy	CI shift
Cl		9123	9122	−24.6
S		9184	9182	−24.0
P		9225	9227	−23.6
Si	$2p_{3/2}-3s_{1/2}$	9267	9272	−23.5
Al		9327	9332	−23.7
Mg		9390	9391	−23.9
Na		9450	9444	−22.4
Ne		9505*	9501	−24.1
Ne	$2p_{3/2}-3p_{1/2}$	9666	9659	−25.6
Fe		9903	9905*	−33.6
Mn		9937	9945*	−33.6
Cr		9975	9978*	−33.5
V		10014	10012	−33.4
Ti		10048	10046	−33.1
Sc		10085	10085	−33.2
Ca	$2p_{3/2}-3d_{5/2}$	10126	10125	−32.9
K		10167	10166	−34.4
Ar		10210	10207	−33.7
Cl		10253	10250*	−31.8
S		10287	10288	−30.5
P		10324	10323	−30.0
Si		10360	10359	−30.2
Al		10406	10404	−31.3
Mg		10452	10448	−33.3
Na		10492	10487	−33.0
Ne		10527	10522	−34.2
Mg		11265	11278*	−42.7
Na	$2p_{1/2}-3s_{1/2}$	11320	11328*	−42.9
Ne		11380	11375	−43.8
Ne	$2p_{1/2}-3d_{3/2}$	12270	12264	−52.2

ing and permits us to model complex electronic systems with reasonable completeness. However, even with this significant reduction in complexity, the complete hybrid structure model for H- to Zn-like Au includes more than 1.5×10^6 levels. Worse, the restrictions on the maximum n of excited states means that some strong dielectronic recombination channels, critical to accurate CSD calculations [12,13], are neglected. We have thus supplemented the hybrid model atomic structure and rate equations with screened hydrogenic superconfigurations for singly and doubly excited states with principal quantum numbers up to $n=10$. The level energies were scaled to agree with ionization potentials from FAC. Rates among the supplemental superconfigurations were calculated following the simplest approximation options described in [39] and were statistically averaged to couple consistently with the fine structure and term levels. The required computational time was reduced by averaging the computed rates among terms in the hybrid model into rates among nonrelativistic configurations before solving the coupled rate equations; the terms are then repopulated following roughly the procedure outlined in Ref. [40]. The repopulation procedure uses configuration-to-hybrid level rates and total configuration populations to determine the populations of levels averaged in the rate matrix solution. It is equivalent to one iteration of a successive refinement matrix solver on an initial population vector whose dominant elements are already converged. This repopulation method restores the individual (nonstatistical) character of levels populated by resonant processes that vary significantly within a configuration. The supplemented hybrid-structure SCRAM model, based on fine structure, term, and superconfiguration energy levels, gives reliable charge state distributions and accurate emission spectra for beam and Maxwellian plasmas with calculations that take about an hour on a 2.4 GHz CPU.

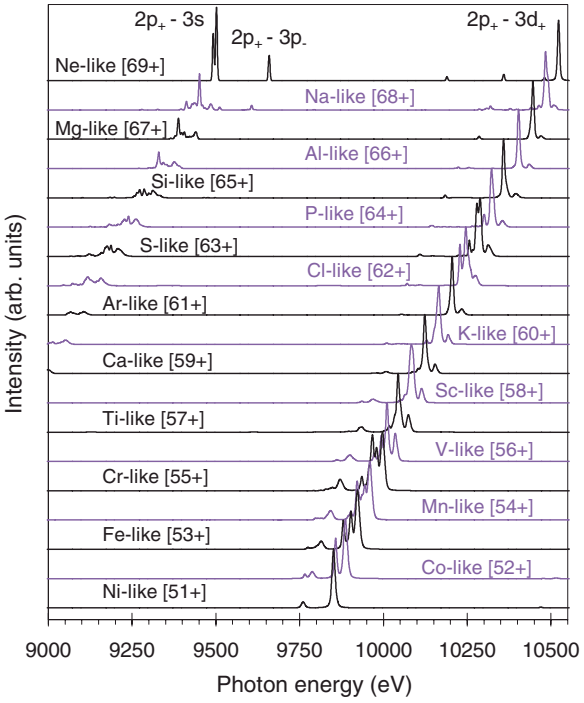

FIG. 3. (Color online) Calculated *L*-shell emission spectra from individual Au ions with a line width ΔE of 1 eV (ten times smaller than the experimental resolution). Each spectrum is normalized to its $2p_+$-$3d_+$ feature.

Figure 3 shows calculated emission from each ion in the range Ni- to Ne-like Au. The imposed linewidth of 1 eV clearly resolves the Ne-like $3G$ ($E1$) and $M2$ lines near 9500 eV that were blended in the experimental spectra and reveals significant structure in the $2p_+-3d_+$ emission features from Cl-like and V- through Co-like Au. The $2p_+-3s$ emission features appearing below 9500 eV are uniformly more complex than the $2p_+-3d_+$ emission features and their relative intensities fall rapidly with decreasing ion charge, in

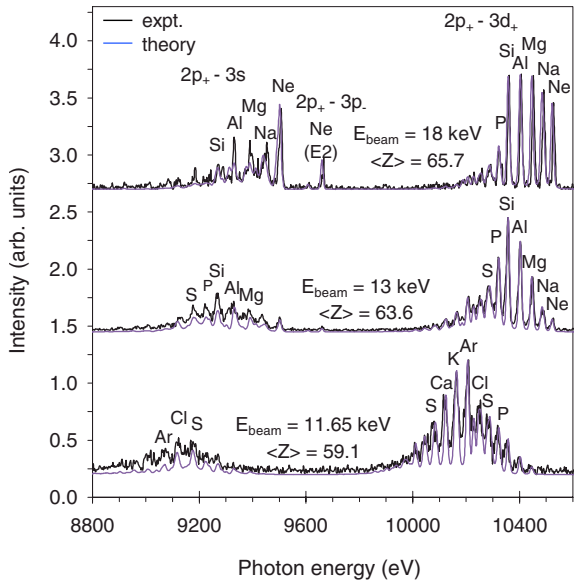

FIG. 4. (Color online) Experimental spectra at three beam energies overlaid with modeled spectra. Strong emission lines are labeled by the isoelectronic sequence of their parent ion.

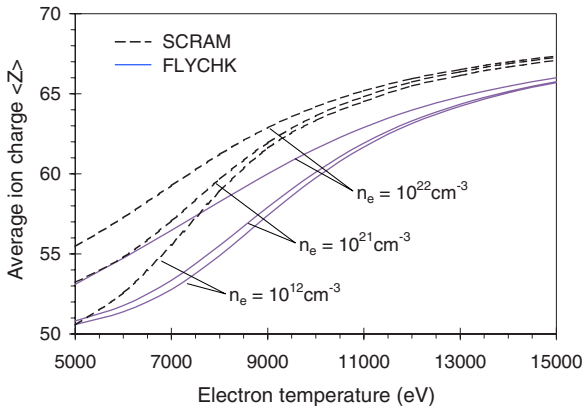

FIG. 5. (Color online) Calculations of the average Au ion charge at various temperatures and densities from the two collisional-radiative models described in the text. The hybrid-structure model SCRAM tends to predict higher $\langle Z \rangle$ and is more sensitive to changes in density than the screened-hydrogenic model FLYCHK.

accordance with the experimental data given in Figs. 1 and 2. These calculations demonstrate that significant spectral structure may be washed out by the 10 eV line width of the present detection system and illustrate the difficulty of assigning a single charge state to a measured emission feature that may be wider than the typical energy separation between charge states.

Comparisons of our model calculations ($\Delta E = 10$ eV) with data collected at three beam energies are given in Fig. 4. For each comparison, we have calculated the charge state distribution using the known beam energy and electron density. We have excluded the supplemental superconfigurations described above, since we have not yet determined how best to represent the spread in level energy which must be convolved with the electron energy distribution of the beam. Including charge exchange processes from some small density of a background neutral gas increases the effective recombination rate and yields average ion charges quite close to the measured values; small adjustments to the initial computed CSDs result in very good agreement with the experimental spectra. (For charge exchange, we assume a neutral ion density of $8-1.5\times10^8$ cm^{-3}, an impact velocity of 2×10^6 cm/s, and allow electron capture through charge exchange to singly excited states with $n=n_{val}+3$.) The resulting average ion charge for each spectrum, ranging from 59.1 to 65.7, are listed on the figure. The charge state distributions are broad, with full widths of 5 to 11 ions. The relative intensities of the Ne-like $2p_+$-$3d_+$ resonance line and the forbidden and intercombination lines $2p_+$-$3p_-$ ($E2$) and $2p_+$-$3s$ ($M2+E1$) are in excellent agreement with the strong Ne-like emission lines in the spectrum with $E_{beam}=18$ keV. Each strong Ne-like feature (including the $E2$ line) is echoed at lower energies by emission features from lower-charged ions. For ions other than Ne-like Au, the modeled spectra tend to underpredict the relative intensities of the $2p_+$-$3s$ emission (this may be partially due to slight differences in the modeled and experimental linewidths). At the lowest beam energy of 11.65 keV, emission from Ar-like ions dominates the $2p_+$-$3d_+$ structure, while the $2p_+$-$3s$ structure remains dominated by emission from higher charge states with lower populations and stronger $2p_+$-$3s$ emission.

IV. DIAGNOSTIC FEATURES

The prominent features identified by ion in Table III can be matched with measured emission spectra to roughly infer the charge state distribution. Diagnosing electron temperatures from measured CSDs and/or average ion charges $\langle Z \rangle$ requires collisional-radiative calculations, which we have provided in Fig. 5. Results for $\langle Z \rangle$ are shown at various temperatures and densities from two different collisional-radiative models: the screened hydrogenic code FLYCHK [39], which includes a complete set of atomic structure and collisional radiative processes for superconfigurations up to $n=10$, and the hybrid-structure model SCRAM described above, with fine structure levels and terms for $n=3-6$ supplemented by screened hydrogenic superconfigurations up to $n=10$. The two codes disagree by a maximum of 4.2 charge states when $n_e=10^{12}$ cm^{-3} and $T_e=9$ keV. When the supplemental superconfigurations are excluded from the SCRAM model, the disagreement with FLYCHK is much larger — up to 10 charge states — due to the dominance of dielectronic recombination. By contrast, excluding the fine structure and term levels from the SCRAM model (leaving only screened hydrogenic levels) improves the agreement with FLYCHK to a maximum difference of 0.3 charge states for $T_e>12$ keV and 2 charge states at lower T_e. The major differences between the models, including the significant density sensitivity of SCRAM at low temperatures, appear thus attributable to the additional detail of the hybrid model's energy levels and rates. In the absence of benchmark ionization balance measurements from well characterized plasmas [41,42], it would be reasonable to use the disagreement between the two models to characterize the uncertainty in electron temperatures diagnosed from a measured CSD. For a

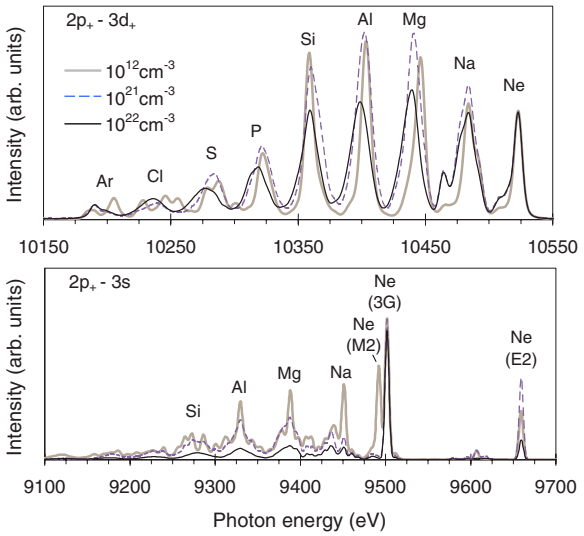

FIG. 6. (Color online) Synthetic *L*-shell spectra at various electron densities calculated with a Maxwellian electron distribution at $T_e=10$ keV and an imposed charge state distribution identical to that used to fit the $E_{beam}=18$ keV spectrum of Fig. 4. Separate plots are given for two spectral regions of interest and all spectra are normalized to the Ne-like $2p_+-3d_+$ ($3D$) resonance line.

given density, this uncertainty of 10–15 % in T_e will generally be larger than the uncertainty in T_e due to assigning $\langle Z\rangle$ by assuming that the population of each ion is directly proportional to its total $2p_+-3d_+$ emission intensity. While that assumption generally holds within 20% for each pair of neighboring ions (with the total $2p_+$-$3d_+$ emission tending to decrease by 5–15 % with each decreasing ion charge for $Au^{+64}-Au^{+51}$), it is complicated by the fact that the emission intensities are not solely dependent on direct excitation and cascades: inner-shell ionization and dielectronic recombination from neighboring ions also contribute to the *L*-shell emission. The exact emission intensity from a given ion thus depends on the populations of neighboring ions as well as the parent ion, so that some uncertainty in the $\langle Z\rangle$ extracted from measured data must be expected unless the modeling is self-consistent.

At temperatures above 10 keV or densities below about 10^{19} cm^{-3}, our calculations are fairly insensitive to n_e. However, at lower temperatures and densities near or above 10^{21} cm^{-3}, the calculated $\langle Z\rangle$ is sensitive to n_e due to increasing populations of multiply excited configurations, as discussed above. Higher densities tend to raise the average ion charge through ladder ionization and also increase the emission of satellite features that differ from the resonant coronal lines only in the configuration of spectator electrons. Figure 6 gives calculated spectra at various densities with identical CSDs, illustrating the effect of increasing satellite intensities on the Au *L*-shell emission. The emission from each ion was calculated at $T_e=10$ keV and folded with the same charge state distribution as used for the EBIT spectrum with $E_{beam}=18$ keV shown in Fig. 4. To maintain validity of comparisons with the beam spectrum, these emission calculations exclude supplemental superconfigurations. With increasing densities, the major transition features are broadened and can be shifted to lower energies by as much as 10 eV as the populations of multiply excited states with weakly bound spectator electrons increase. UTA widths (excluded here to highlight the energy shifts) will further obscure the clear picket-fence pattern at the higher densities. The density-dependent shifting and broadening effects can appear well before the average ion charge is driven higher by ladder ionization, and may be useful as density signatures in measurements with high spectral resolution.

For plasmas with significant Ne-like Au populations, the metastable line intensities provide another potential density diagnostic. Increasing densities tend to destroy weak forbidden lines by collisionally depopulating the upper level of the transitions. Our calculations show that the $M2$ line disappears well before the density reaches 10^{21} cm^{-3} and that the $3G$ line begins to decrease at an electron density of 10^{22} cm^{-3} towards its LTE intensity of $0.06\times 3D$. The forbidden $E2L$ line at 9659 eV has a more complex behavior: even though its radiative decay rate is 150 times smaller than that of the $3G$ transition, its intensity relative to the other Ne-like lines *increases* with density up to some maximum before it begins a rapid decrease due to collisional destruction.

V. CONCLUSIONS

The experimental data presented here from the SuperEBIT electron beam ion trap reveal the core-excitation spectra of Au at a resolution that clearly separates the dominant features from individual charge states, thus providing an immediate diagnostic tool for the study of other hot plasmas. Complementing the experimental data with theory and collisional-radiative modeling, the diagnostic value of the data is much enhanced. The FAC atomic structure code has proven to give very reliable transition data, calculating transition energies to within some 0.05% of the experimental data even with the configuration interaction restricted to coronal levels. The ≈5 eV maximum discrepancy in transition energies is much smaller than the typical separation of emission features from different charge states and has allowed us to overcome an earlier uncertainty in the identification of emission features in the spectra of high-*Z* ions [16]. Collisional-radiative calculations of $\langle Z\rangle$ from two codes are provided to facilitate temperature diagnostics from measured charge state distributions. Finally, the effects of electron density on *L*-shell Au emission features have been investigated. Future refinements of non-LTE collisional-radiative calculations may enable greater precision in temperature diagnostics, and investigations are underway into both the anomalous density behavior of the forbidden $2p_{3/2}-3p_{1/2}$ E2L line at 9659 eV and dielectronic recombination of beam electrons into exotic multiply excited states, the decays of which may contribute to emission lines above the electron beam energy. The information presented here should enable researchers to infer approximate electron temperatures and densities from measured *L*-shell emission from highly ionized Au in hot plasmas.

ACKNOWLEDGMENTS

This work was performed under the auspices of the U.S.

Department of Energy by Lawrence Livermore National Laboratory in part under Contract No. W-7405-Eng-48 and in part under Contract No. DE-AC52-07NA27344. G.V.B., S.B.H., H.K.C., and K.W. were supported in part by Contract No. LLNL LDRD 05-erd-068. E.T. acknowledges travel support from the German Research Association (DFG). We gratefully acknowledge valuable discussions with J. Bauche, C. Bauche-Arnoult, M. J. May, and C. J. Fontes.

[1] D. E. Hinkel, M. B. Schneider, H. A. Baldis, G. Bonanno, D. E. Bower, K. M. Campbell, J. R. Celeste, S. Compton, R. Costa, E. L. Dewald, S. N. Dixit, M. J. Eckart, D. C. Eder, M. J. Edwards, A. Ellis, J. A. Emig, D. H. Froula, S. H. Glenzer, D. Hargrove, C. A. Haynam, R. F. Heeter, M. A. Henesian, J. P. Holder, G. Holtmeier, L. James, K. S. Jancaitis, D. H. Kalantar, J. H. Kamperschroer, R. L. Kauffman, J. Kimbrough, R. K. Kirkwood, A. E. Koniges, O. L. Landen, M. Landon, A. B. Langdon, F. D. Lee, B. J. MacGowan, A. J. Mackinnon, K. R. Manes, C. Marshall, M. J. May, J. W. McDonald, J. Menapace, E. I. Moses, D. H. Munro, J. R. Murray, C. Niemann, D. Pellinen, V. Rekow, J. A. Ruppe, J. Schein, R. Shepherd, M. S. Singh, P. T. Springer, C. H. Still, L. J. Suter, G. L. Tietbohl, R. E. Turner, B. M. Van Wonterghem, R. J. Wallace, A. Warrick, P. Watts, F. Weber, P. J. Wegner, E. A. Williams, B. K. Young, and P. E. Young, Phys. Plasmas **12**, 056305 (2005).

[2] D. E. Hinkel, M. B. Schneider, B. K. Young, A. B. Langdon, E. A. Williams, M. D. Rosen, and L. J. Suter, Phys. Rev. Lett. **96**, 195001 (2006).

[3] J. Lindle, Phys. Plasmas **2**, 3933 (1995).

[4] P. Beiersdorfer, M. Bitter, S. von Goeler, S. Cohen, K. W. Hill, J. Timberlake, R. S. Walling, M. H. Chen, P. L. Hagelstein, and J. H. Scofield, Phys. Rev. A **34**, 1297 (1986).

[5] P. Beiersdorfer, S. von Goeler, M. Bitter, E. Hinnov, R. Bell, S. Bernabei, J. Felt, K. W. Hill, R. Hulse, J. Stevens, S. Suckewer, J. Timberlake, A. Wouters, M. H. Chen, J. H. Scofield, D. D. Dietrich, M. Gerassimenko, E. Silver, R. S. Walling, and P. L. Hagelstein, Phys. Rev. A **37**, 4153 (1988).

[6] M. J. May, K. B. Fournier, P. Beiersdorfer, H. Chen, and K. L. Wong, Phys. Rev. E **68**, 036402 (2003).

[7] P. Neill, C. Harris, A. S. Safronova, S. Hamasha, S. Hansen, U. I. Safronova, and P. Beiersdorfer, Can. J. Phys. **82**, 931 (2004).

[8] M. J. May, P. Beiersdorfer, N. Jordan, J. H. Scofield, K. J. Reed, S. B. Hansen, K. B. Fournier, M. F. Gu, G. V. Brown, F. S. Porter, R. Kelley, C. A. Kilbourne, and K. R. Boyce, Nucl. Instrum. Methods Phys. Res. B **235**, 231 (2005).

[9] J. F. Seely, C. A. Back, C. Constantin, R. W. Lee, H.-K. Chung, L. T. Hudson, C. I. Szabo, A. Henins, G. E. Holland, R. Atkin, and L. Marlin, J. Quant. Spectrosc. Radiat. Transf. **99**, 572 (2006).

[10] M. J. May, M. B. Schneider, H.-K. Chung, and D. E. Hinkel, Report No. UCRL-JRNL-214752, 2005 (unpublished); M. J. May, M. B. Schneider, S. B. Hansen, H.-K. Chung, D. E. Hinkel, H. A. Baldis, and C. Constantin, Report No. LLNL-JRNL-402122, 2008 (unpublished).

[11] R. W. Lee, J. K. Nash, and Y. Ralchenko, J. Quant. Spectrosc. Radiat. Transf. **58**, 131 (1997).

[12] C. Bowen, A. Decoster, C. J. Fontes, K. B. Fournier, O. Peyrusse, and Yu. V. Ralchenko, J. Quant. Spectrosc. Radiat. Transf. **81**, 71 (2003).

[13] C. Bowen, R. W. Lee, and Yu. Ralchenko, J. Quant. Spectrosc. Radiat. Transf. **99**, 102 (2006).

[14] D. A. Knapp, R. E. Marrs, S. R. Elliott, E. W. Magee, and R. Zasadzinski, Nucl. Instrum. Methods Phys. Res. A **334**, 305 (1993).

[15] P. Beiersdorfer, Can. J. Phys. **86**, 1 (2008).

[16] M. B. Schneider, R. Mancini, K. Widmann, K. B. Fournier, G. V. Brown, H.-K. Chung, H. A. Baldis, K. Cone, S. B. Hansen, M. J. May, D. Thorn, and P. Beiersdorfer, Can. J. Phys. **86**, 259 (2008).

[17] A. M. Niles, E. W. Magee, D. B. Thorn, G. V. Brown, H. Chen, and P. Beiersdorfer, Rev. Sci. Instrum. **77**, 10F106 (2006).

[18] F. S. Porter, M. D. Audley, P. Beiersdorfer, K. R. Boyce, R. P. Brekosky, G. V. Brown, K. C. Gendreau, J. Gygax, S. Kahn, R. L. Kelley, C. K. Stahle, and A. E. Szymkowiak, Proc. SPIE **4140**, 407 (2000).

[19] F. S. Porter, G. V. Brown, K. R. Boyce, R. L. Kelley, C. A. Kilbourne, P. Beiersdorfer, H. Chen, S. Terracol, S. M. Kahn, and A. E. Szymkowiak, Rev. Sci. Instrum. **75**, 3772 (2004).

[20] F. S. Porter, P. Beiersdorfer, K. R. Boyce, G. V. Brown, H. Chen, J. Gygax, S. M. Kahn, R. L. Kelley, C. A. Kilbourne, E. Magee, D. B. Thorn, Can. J. Phys. **86**, 231 (2008).

[21] R. L. Kelley *et al.*, Publ. Astron. Soc. Jpn. **59**, 77 (2007).

[22] K. R. Boyce, M. D. Audley, R. G. Baker, J. J Dumonthier, R. Fujimoto, K. C. Gendreau, Y. Ishisaki, R. L. Kelley, C. K. Stahle, A. E. Szymkowiak, and G. E. Winkert, Proc. SPIE **3765**, 741 (1999).

[23] J. D. Garcia and J. E. Mack, J. Opt. Soc. Am. **55**, 654 (1965).

[24] G. W. F. Drake, Can. J. Phys. **66**, 586 (1988).

[25] J. H. Scofield (private communications), calculated values.

[26] On the web at http://www-cxro.lbl.gov/

[27] A. H. Gabriel, Mon. Not. R. Astron. Soc. **160**, 99 (1972).

[28] P. Beiersdorfer, R. E. Marrs, J. R. Henderson, D. A. Knapp, M. A. Levine, D. B. Platt, M. B. Schneider, D. A. Vogel, and K. L. Wong, Rev. Sci. Instrum. **61**, 2338 (1990); P. Beiersdorfer, M. H. Chen, R. E. Marrs, and M. A. Levine, Phys. Rev. A **41**, 3453 (1990); P. Beiersdorfer, Nucl. Instrum. Methods Phys. Res. B **56/57**, 1144 (1991); (unpublished).

[29] M. J. Vilkas, Y. Ishikawa, and E. Träbert, Eur. Phys. J. D **41**, 77 (2006).

[30] E. P. Ivanova and A. V. Gulov, At. Data Nucl. Data Tables **49**, 1 (1991).

[31] H. L. Zhang, D. H. Sampson, R. E. H. Clark, and J. B. Mann, At. Data Nucl. Data Tables **37**, 17 (1987).

[32] H. L. Zhang and D. H. Sampson, At. Data Nucl. Data Tables **43**, 1 (1989).

[33] H. L. Zhang and D. H. Sampson, At. Data Nucl. Data Tables **41**, 1 (1989).

[34] D. H. Sampson and H. L. Zhang, Phys. Rev. A **36**, 3590 (1987).

[35] A. Bar-Shalom, M. Klapisch, and J. Oreg, J. Quant. Spectrosc.

Radiat. Transf. **71**, 169 (2001).
[36] M. F. Gu, Astrophys. J. **582**, 1241 (2003).
[37] M. F. Gu, Can. J. Phys. (to be published).
[38] S. B. Hansen, J. Bauche, C. Bauche-Arnoult, and M. F. Gu, High Energy Density Phys. **3**, 109 (2007).
[39] H. K. Chung, M. H. Chen, W. L. Morgan, Y. Ralchenko, and R. W. Lee, High Energy Density Phys. **1**, 3 (2005).
[40] F. B. Rosmej, Europhys. Lett. **76**, 1081 (2006).
[41] K. L. Wong, M. J. May, P. Beiersdorfer, K. B. Fournier, B. Wilson, G. V. Brown, P. Springer, P. A. Neill, and C. L. Harris, Phys. Rev. Lett. **90**, 235001 (2003).
[42] R. F. Heeter, S. B. Hansen, K. B. Fournier, M. E. Foord, D. H. Froula, A. J. Mackinnon, M. J. May, M. B. Schneider, and B. K. F. Young, Phys. Rev. Lett. **99**, 195001 (2007).